Magnon Hall effect and topology in kagome lattices: A theoretical investigation

Alexander Mook,[1] Jürgen Henk,[2] and Ingrid Mertig[1,2]
[1]*Max-Planck-Institut für Mikrostrukturphysik, D-06120 Halle (Saale), Germany*
[2]*Institut für Physik, Martin-Luther-Universität Halle-Wittenberg, D-06099 Halle (Saale), Germany*
(Received 21 January 2014; revised manuscript received 27 March 2014; published 14 April 2014)

Ferromagnetic insulators with Dzyaloshinskii-Moriya interaction show the magnon Hall effect, i.e., a transverse heat current upon application of a temperature gradient. In this theoretical investigation we establish a close connection of the magnon Hall effect in two-dimensional kagome lattices with the topology of their magnon dispersion relation. From the topological phase diagram we predict systems which show a change of sign in the heat current in dependence on temperature. Furthermore, we derive the high-temperature limit of the thermal Hall conductivity; this quantity provides a figure of merit for the maximum strength of the magnon Hall effect. Eventually, we compare the temperature and field dependence of the magnon Hall conductivity of the three-dimensional pyrochlore $Lu_2V_2O_7$ with experimental results.

DOI: 10.1103/PhysRevB.89.134409 PACS number(s): 66.70.−f, 75.30.−m, 75.47.−m, 85.75.−d

I. INTRODUCTION

The Hall and Nernst effects comprise a variety of phenomena, all showing a transverse current in response to a longitudinal external field [1–3]. In the case of Hall effects, this field is (typically) an applied voltage, whereas in the case of Nernst effects, this is a temperature gradient. For the conventional and anomalous effects, one observes an electric current; a spin current is measured for their "spin" counterparts, e.g., the spin Hall effect. Typically, one associates the observation of a transverse current with the term Hall effect or Hall geometry, rather than with a Nernst effect or Nernst geometry. An example of this notation is the phonon Hall effect [4] which describes a heat current perpendicular to a longitudinal temperature gradient.

The diversity of Hall effects has been extended by Onose *et al.* who discovered the magnon Hall effect (MHE) [5]. For the insulating ferromagnet $Lu_2V_2O_7$ with pyrochlore lattice [Fig. 1(a)] they found a transverse heat current upon application of a longitudinal temperature gradient. Theoretical understanding of this phenomenon has been provided by Matsumoto and Murakami, who explained the magnon Hall effect as a consequence of noncompensated magnon edge currents in a two-dimensional system [6,7]. Later on, Zhang *et al.* recognized that this net edge current results from the topology of the system, thereby confirming the existence of topological magnon insulators [8].

The magnon Hall effect is due to the spin-orbit interaction. In a magnetic system without inversion center—as in the pyrochlore lattice—it results in the Dzyaloshinskii-Moriya contribution to the exchange interaction of localized magnetic moments which opens up band gaps in the magnon dispersion relation. These avoided crossings give a nonzero Berry curvature and nonzero topological invariants (i.e., the Chern numbers). The transverse thermal conductivity κ^{xy} is consequently expressed as an integral of the Berry curvature over the Brillouin zone. The preceding information reveals a close similarity to the physics of electronic topological insulators in which spin-orbit-induced band inversions yield nonzero topological invariants and topologically protected surface or edge states [9–11]. The transverse thermal conductivity of the MHE is, thus, in line with several other—mostly electronic—physical quantities that are expressed in terms of the Berry curvature and have been studied extensively in the past [12,13].

Although the fundamental physics of the MHE has been derived by Matsumoto and Murakami [6,7], a number of open questions needs to be answered. In our theoretical investigation reported in this paper we deduce a topological phase diagram for kagome systems. It turns out that for specific systems the transverse thermal conductivity changes sign in dependence on temperature; this implies that the orientation of the heat current can be reversed by tuning the temperature in a device. Furthermore, we derive the high-temperature limit of the thermal conductivity which provides a figure of merit for the strength of the magnon Hall effect. To come closer to experiment, we extend our analysis of two-dimensional lattices to the three-dimensional pyrochlore lattice by stacking noninteracting kagome layers. By comparison of the temperature and field dependence of the magnon Hall conductivity with the experimental results of Onose *et al.* [5], we determine the Dzyaloshinskii-Moriya parameters of $Lu_2V_2O_7$.

The paper is organized as follows. In Sec. II we outline the quantum-mechanical description of magnons in kagome lattices (Sec. II A) and derive an expression for the transverse thermal conductivity (Sec. II B). Results are presented in Sec. III: topology and magnon band structure (Sec. III A), the topological phase diagram (Sec. III B), the high-temperature limit of the thermal conductivity (Sec. III C), and a comparison with experiments for $Lu_2V_2O_7$ (Sec. III D). We conclude with Sec. IV.

II. THEORY OF THE MAGNON HALL EFFECT

A. Model Hamiltonian for magnons

For the description of magnons in kagome lattices, we use the quantum-mechanical Heisenberg model [14]. In the Hamiltonian

$$\mathcal{H}_{\mathrm{H}} = -\frac{1}{2}\sum_{n\neq m} J_m^n \hat{\mathbf{s}}_m \cdot \hat{\mathbf{s}}_n \tag{1}$$

spin operators $\hat{\mathbf{s}}_n$ and $\hat{\mathbf{s}}_m$ at lattice sites n and m are coupled by exchange parameters J_m^n. The latter account for

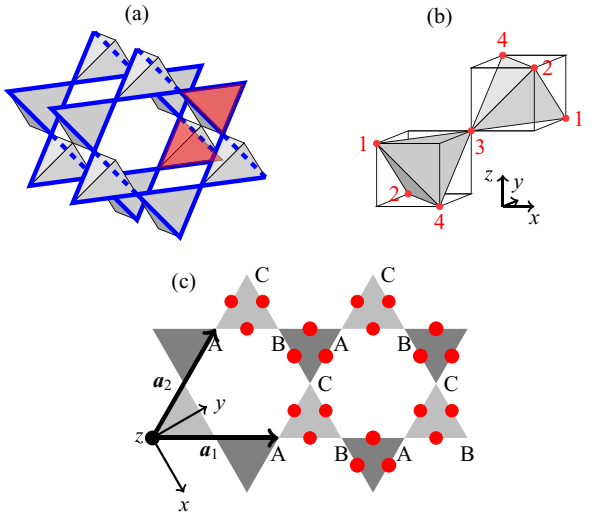

FIG. 1. (Color online) Pyrochlore and kagome lattices. (a) Three-dimensional pyrochlore lattice, with (111) planes representing stacked two-dimensional kagome lattices (marked by blue bold lines). (b) Atomic positions, labeled by numbers, in the pyrochlore lattice. (c) Two-dimensional kagome lattice with lattice vectors $\boldsymbol{a}_1$ and $\boldsymbol{a}_2$. Atoms A, B, and C are placed at the corners of the triangles. Dzyaloshinskii-Moriya vectors are aligned normal to the lattice plane and are represented by red dots: along $+z$ ($-z$) for a counterclockwise (clockwise) chirality: A-B-C (C-B-A).

isotropic symmetric spin-spin interactions, typically termed "Heisenberg" exchange. The eigenvectors of $\mathcal{H}_{\mathrm{H}}$,

$$|\boldsymbol{k}\rangle = \frac{1}{\sqrt{N}} \sum_m e^{\mathrm{i}\boldsymbol{k}\cdot\boldsymbol{R}_m} |\boldsymbol{R}_m\rangle, \tag{2}$$

are called "one-magnon states", where N is the total number of spins, $\boldsymbol{R}_m$ is the vector pointing to lattice site m, and $|\boldsymbol{R}_m\rangle$ denotes the state with all spins aligned along the ferromagnetic ground state except the one at lattice site m; its z component is reduced by $\hbar$.

As mentioned above, the spin-orbit interaction is essential for the MHE; it contributes in two ways to the Hamiltonian: the magnetocrystalline anisotropy, which is not considered in this paper, and the Dzyaloshinskii-Moriya interaction [15,16]. The Dzyaloshinskii-Moriya (DM) contribution is anisotropic as well as antisymmetric and can be written as

$$\mathcal{H}_{\mathrm{DM}} = \frac{1}{2} \sum_{m \neq n} \boldsymbol{D}_m^n (\hat{\boldsymbol{s}}_m \times \hat{\boldsymbol{s}}_n). \tag{3}$$

$\boldsymbol{D}_m^n$ is the DM vector between sites m and n ($\boldsymbol{D}_m^n = -\boldsymbol{D}_n^m$).

The coupling to an external magnetic field $\boldsymbol{H}$ is introduced by a Zeeman term,

$$\mathcal{H}_{\mathrm{ext}} = -g\mu_{\mathrm{B}} \sum_n \boldsymbol{H} \cdot \hat{\boldsymbol{s}}_n. \tag{4}$$

g and μ_{B} denote the g factor of electrons and Bohr's magneton, respectively. The complete Hamiltonian then reads

$$\mathcal{H} = \mathcal{H}_{\mathrm{H}} + \mathcal{H}_{\mathrm{DM}} + \mathcal{H}_{\mathrm{ext}}. \tag{5}$$

For the time being, we consider only one-magnon states and, thereby, exclude the kinematic [17] interaction that originates from the impossibility of locating more than $2s$ deviations at a single spin s. We also do not account for the dipole-dipole interaction and for higher-order spin interactions (e.g., Ref. [18]).

By means of Moriya's symmetry rules [16], the DM vectors of the pyrochlore lattice can be expressed as

$$\begin{aligned} \boldsymbol{D}_{12} &= \frac{\widetilde{D}}{\sqrt{2}}(-\boldsymbol{y} - \boldsymbol{z}), \quad \boldsymbol{D}_{13} = \frac{\widetilde{D}}{\sqrt{2}}(-\boldsymbol{x} + \boldsymbol{y}), \\ \boldsymbol{D}_{14} &= \frac{\widetilde{D}}{\sqrt{2}}(\boldsymbol{x} + \boldsymbol{z}), \quad \boldsymbol{D}_{24} = \frac{\widetilde{D}}{\sqrt{2}}(-\boldsymbol{x} - \boldsymbol{y}), \\ \boldsymbol{D}_{43} &= \frac{\widetilde{D}}{\sqrt{2}}(-\boldsymbol{y} + \boldsymbol{z}), \quad \boldsymbol{D}_{23} = \frac{\widetilde{D}}{\sqrt{2}}(\boldsymbol{x} - \boldsymbol{z}), \end{aligned} \tag{6}$$

where $\widetilde{D}$ denotes the DM constant of adjacent sites. The site labels 1–4 and the unit vectors $\boldsymbol{x}$, $\boldsymbol{y}$, and $\boldsymbol{z}$ of the Cartesian coordinate system are defined in Fig. 1(b) (cf. Refs. [19] and [20]).

In the experiment by Onose *et al.* [5], an external magnetic field $\boldsymbol{H}$ is applied along the [111] direction. Only the components of the DM vectors along this direction contribute to the MHE; the other components do not contribute up to second order in the spin deviation from the [111] direction (cf. the supplemental online material of Ref. [5]). With $\sqrt{3}\boldsymbol{n} = \boldsymbol{x} + \boldsymbol{y} + \boldsymbol{z}$ we arrive at

$$D \equiv -\boldsymbol{n} \cdot \boldsymbol{D}_{12} = \boldsymbol{n} \cdot \boldsymbol{D}_{14} = -\boldsymbol{n} \cdot \boldsymbol{D}_{24} = \frac{2}{\sqrt{6}} \widetilde{D}, \tag{7a}$$

$$0 = \boldsymbol{n} \cdot \boldsymbol{D}_{13} = \boldsymbol{n} \cdot \boldsymbol{D}_{23} = \boldsymbol{n} \cdot \boldsymbol{D}_{43}. \tag{7b}$$

Hence, only spins at sites that form a kagome lattice within the (111) plane are coupled by the DM interaction (here, sites 1, 2, and 4). This suggests a study of (two-dimensional) kagome lattices instead of (three-dimensional) pyrochlore lattices, as is done in this paper.

To simplify the calculation for the kagome lattice, we use the coordinate system shown in Fig. 1(c), in which the kagome lattice and the xy plane coincide and the [111] direction is along z. The lattice vectors read

$$\boldsymbol{a}_1 = (1, \sqrt{3})\frac{a}{2}, \tag{8a}$$

$$\boldsymbol{a}_2 = (-1, \sqrt{3})\frac{a}{2} \tag{8b}$$

(a is the lattice constant) in Cartesian coordinates. The DM vectors are then along the z direction. Their orientation is given by the chirality of the triangles in the kagome lattice: those with counterclockwise (clockwise) chirality point along the $+z$ ($-z$) direction [cf. the red dots in Fig. 1(c)]. The length of the DM vectors is D.

By means of ladder operators $\hat{s}^{\pm} \equiv \hat{s}^x \pm \mathrm{i}\hat{s}^y$ and the definition

$$\tilde{J}_m^n \exp\left(\mathrm{i}\phi_m^n\right) \equiv J_m^n + \mathrm{i}D_m^n \tag{9}$$

the Hamiltonian reads [5]

$$\begin{aligned} \mathcal{H} = &-\frac{1}{4} \sum_{m \neq n} \tilde{J}_m^n \left[e^{\mathrm{i}\phi_m^n} \hat{s}_m^- \hat{s}_n^+ + e^{-\mathrm{i}\phi_m^n} \hat{s}_m^+ \hat{s}_n^- \right] \\ &- \frac{1}{2} \sum_{m \neq n} J_m^n \hat{s}_m^z \hat{s}_n^z - g\mu_{\mathrm{B}} H \sum_m \hat{s}_m^z. \end{aligned} \tag{10}$$

H is the strength of the external magnetic field.

From Eq. (9) it is obvious that a magnon accumulates an additional phase ϕ_m^n upon propagation from site m to n, which is brought about by the spin-orbit interaction. This can be viewed as a result of a textured flux within the plaquettes of the kagome lattice [21], similar to the Haldane model for an electronic topological insulator [22]. Thus, we are concerned with a nonzero Berry curvature $\boldsymbol{\Omega}(\boldsymbol{k})$ (Ref. [23]) and with topological invariants.

For a given set of parameters $\{J_m^n, D_m^n\}$, we solve the eigenproblem of the complete Hamiltonian $\mathcal{H}$, yielding the magnon dispersion relations $\varepsilon_i(\boldsymbol{k})$ [wave vector $\boldsymbol{k} = (k_x, k_y, 0)$, band index i] and the Berry curvature

$$\boldsymbol{\Omega}_j(\boldsymbol{k}) \equiv \mathrm{i} \sum_{i \neq j} \frac{\langle i(\boldsymbol{k})|\nabla_{\boldsymbol{k}}\mathcal{H}(\boldsymbol{k})|j(\boldsymbol{k})\rangle \times \langle j(\boldsymbol{k})|\nabla_{\boldsymbol{k}}\mathcal{H}(\boldsymbol{k})|i(\boldsymbol{k})\rangle}{[\varepsilon_i(\boldsymbol{k}) - \varepsilon_j(\boldsymbol{k})]^2}. \tag{11}$$

$|i(\boldsymbol{k})\rangle$ and $\varepsilon_i(\boldsymbol{k})$ are the eigenvectors and eigenvalues of $\mathcal{H}$, respectively.

B. Transverse thermal conductivity and Chern numbers

Having solved the magnon Hamiltonian, the transverse thermal conductivity can be computed as follows. By formulating semiclassical equations of motion for magnon wave packets which include the anomalous velocity in terms of the Berry curvature, the intrinsic contribution[1] to the transverse thermal conductivity is expressed as

$$\kappa^{xy} = \frac{k_B^2 T}{(2\pi)^2 \hbar} \sum_i \int_{\mathrm{BZ}} c_2(\varrho_i)\, \Omega_i^z(\boldsymbol{k})\, dk^2. \tag{12}$$

The sum runs over all bands i in the magnon dispersion relation, and the integral is over the Brillouin zone (BZ). The Bose distribution function ϱ_i enters the function c_2 which is given by

$$c_2(x) \equiv (1+x)\left(\ln\frac{1+x}{x}\right)^2 - (\ln x)^2 - 2\,\mathrm{Li}_2(-x). \tag{13}$$

Li_2 is the dilogarithm or Spence function [6,7]. c_2 is depicted in Fig. 2; it accounts via the Bose distribution for the temperature dependence of κ^{xy}.

The transverse thermal conductivity and the Chern number of band i,

$$C_i \equiv \frac{1}{2\pi} \int_{\mathrm{BZ}} \Omega_i^z(\boldsymbol{k})\, dk^2, \tag{14}$$

differ by constant factors and by the c_2 function in the integrand. This establishes a close connection of the magnon Hall effect with the topology of the magnon dispersion relation in the kagome lattice.

C. Numerical aspects

To calculate the Chern numbers and the transverse thermal conductivity [cf. Eqs. (14) and (12)], a k-space integration has to be performed. All results of this paper are obtained for Gaussian meshes with 2500 points. This gives an accuracy of the (integer) Chern numbers better than 10^{-5}. For almost closed band gaps the Berry curvature gets locally very large [cf. the denominator in Eq. (11)]; in these cases, a refined mesh has to be used: 40 000 points for band gaps less than 0.1 meV.

[1]The skew scattering contribution is not considered in this paper.

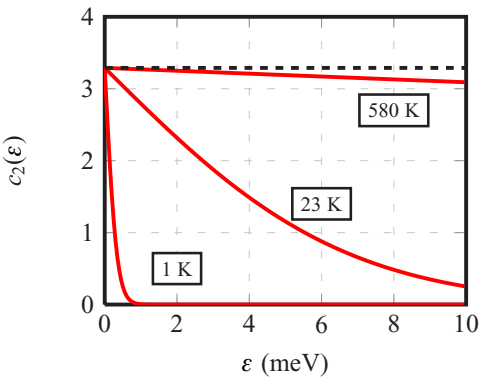

FIG. 2. (Color online) Function $c_2(\varepsilon)$, as defined in Eq. (13), versus energy ε for selected temperatures (as indicated). The broken line marks the high-temperature limit of $\pi^2/3 \approx 3.289\,87$.

III. RESULTS AND DISCUSSION

In the following analysis we assume a kagome lattice with all three basis atoms being identical, i.e., identical spin and exchange parameters. We consider the Heisenberg exchange between nearest (J_{N}) and next-nearest (J_{NN}) sites; the Dzyaloshinskii-Moriya parameters account only for nearest-neighbor interactions (D).

A. Magnon dispersion relation and topological invariants

First, we address the close connection of the magnon band structure, the Chern numbers, and the thermal conductivity. For this purpose, we introduce Chern numbers of isoenergy surfaces

$$C_i(\varepsilon) \equiv \frac{1}{2\pi} \int_{\mathrm{BZ}} \delta(\varepsilon_i - \varepsilon)\, \Omega_i^z(\boldsymbol{k})\, dk^2 \tag{15}$$

[cf. Eq. (14)] and the corresponding energy-dependent contribution to the transverse thermal conductivity

$$\kappa^{xy}(\varepsilon) = \frac{k_B^2 T}{(2\pi)^2 \hbar} \sum_i \int_{\mathrm{BZ}} \delta(\varepsilon_i - \varepsilon)\, c_2(\varrho_i)\, \Omega_i^z(\boldsymbol{k})\, dk^2 \tag{16}$$

[cf. Eq. (12)].

Inspection of Fig. 3 provides that the main contributions to the Chern numbers appear at the band edges of spin-orbit-induced band gaps, that is, where the Berry curvature is largest [cf. the denominator in Eq. (11)]. The total Chern numbers are $C_1 = 1$, $C_2 = 0$, and $C_3 = -1$, indicating that the topological phase of the magnon dispersion is characterized by $(1, 0, -1)$ (the sum over all Chern numbers is zero in any case).

Because the thermal conductivity is mainly given by the Chern numbers weighted by the c_2 function, $\kappa^{xy}(\varepsilon)$ shows the same features as the Chern numbers. However, it decreases towards higher energies due to the energy dependence of c_2 (see Fig. 2). Furthermore, adjacent peaks show opposite signs, leading to a partial cancellation in the total conductivity.

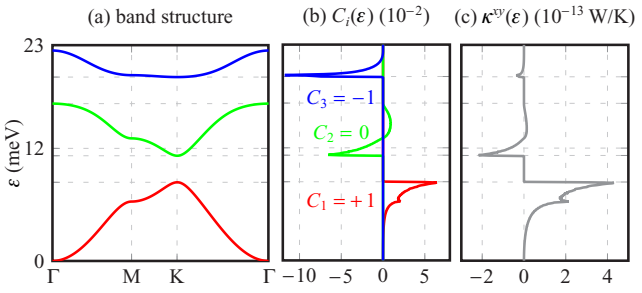

FIG. 3. (Color online) Relation between magnon band structure, Chern numbers, and thermal conductivity. The magnon dispersion relation for $J_N = 4$ meV, $D = 1$ meV, and $J_{NN} = 0$ is shown in (a). The band- and energy-resolved Chern numbers $C_i(\varepsilon)$ and the energy-resolved thermal conductivity $\kappa^{xy}(\varepsilon)$ at $T = 30$ K are displayed in (b) and (c), respectively. The step width of the energy mesh is $1/20$ meV. The energy scale is compressed to account for the finite temperature (cf. Sec. III D).

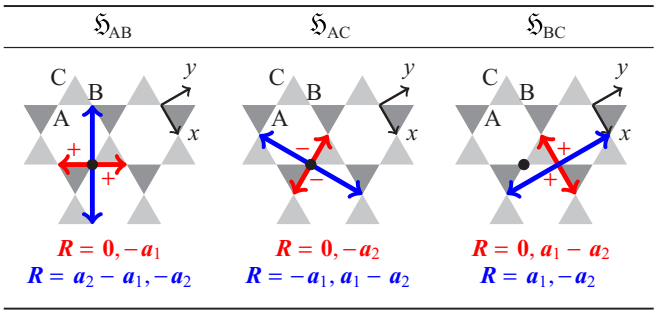

FIG. 4. (Color online) Dzyaloshinskii-Moriya interaction in a kagome lattice. Lattice vectors $\boldsymbol{R}$ from atom $i = $ A,B,C to the basis of both nearest (red) and next-nearest (blue) neighbors of type $j = $ A,B,C are given by arrows. $\pm$ represent the signs of the Dzyaloshinskii-Moriya interaction, in accordance with the chirality. Lattice vectors $\boldsymbol{a}_1$ and $\boldsymbol{a}_2$ are defined in Fig. 1(c). The dot (•) denotes the origin of the coordinate system.

These findings suggest a way to maximize the thermal conductivity. The requirements comprise (i) a wide energy gap provided by (ii) a large DM constant to obtain large c_2 differences for the band edges, and (iii) a flat first band for a large c_2. These features yield an absolute boundary of the transverse thermal conductivity at low temperatures. Considering only the first band, i.e., assuming a wide band gap, and approximating the lowest band by $\varepsilon_1(\boldsymbol{k}) = 0$, for which $c_2(0) = \pi^2/3$ (Fig. 2), one arrives at

$$|\kappa^{xy}| = \left|\sum_n \kappa_n^{xy}\right| < \left|\kappa_1^{xy}\right| < \frac{k_B^2 \pi}{6\hbar} T |C_1|, \tag{17}$$

where C_1 is the Chern number of the first band.

B. Topological phase diagram

A topological phase transition is closely related to a band inversion that appears due to a variation of parameters that enter the Hamiltonian: a band gap closes and reopens again, which is accompanied by a (discrete) change of the respective topological invariants (cf. Ref. [24] for an electronic topological insulator). In this section, we discuss the topological phase diagram of the magnon Hamiltonian. Each system is characterized by a set of constants D, J_N, and J_{NN}, from which a point $(J_{NN}/J_N, D/J_N)$ in phase space is defined. It is conceivable that deformation of the lattice or magnetic doping are means to change the topological phase. Some regions of the phase diagram cannot be realized in practice because $D < J_N$ in real systems.

To derive phase boundaries, we write the Hamiltonian as a 3×3 matrix,

$$\mathfrak{H}(\boldsymbol{k}) = \begin{pmatrix} \mathfrak{H}_{AA}(\boldsymbol{k}) & \mathfrak{H}_{AB}(\boldsymbol{k}) & \mathfrak{H}_{AC}(\boldsymbol{k}) \\ \mathfrak{H}_{AB}^*(\boldsymbol{k}) & \mathfrak{H}_{AA}(\boldsymbol{k}) & \mathfrak{H}_{BC}(\boldsymbol{k}) \\ \mathfrak{H}_{AC}^*(\boldsymbol{k}) & \mathfrak{H}_{BC}^*(\boldsymbol{k}) & \mathfrak{H}_{AA}(\boldsymbol{k}) \end{pmatrix}, \tag{18}$$

with A, B, and C indicating the basis atoms (cf. Figs. 1 and 4). The matrix elements read

$$\mathfrak{H}_{AA}(\boldsymbol{k}) = 0, \tag{19}$$

$$\mathfrak{H}_{AB}(\boldsymbol{k}) = -(J_N + iD)s(1 + e^{i(-k_x - \sqrt{3}k_y)/2}) - J_{NN}s(e^{-ik_x} + e^{i(k_x - \sqrt{3}k_y)/2}), \tag{20}$$

$$\mathfrak{H}_{AC}(\boldsymbol{k}) = -(J_N - iD)s(1 + e^{i(k_x - \sqrt{3}k_y)/2}) - J_{NN}s(e^{ik_x} + e^{i(-k_x - \sqrt{3}k_y)/2}), \tag{21}$$

$$\mathfrak{H}_{BC}(\boldsymbol{k}) = -(J_N + iD)s(1 + e^{ik_x}) - 2J_{NN}s e^{ik_x/2} \cos\left(\frac{\sqrt{3}}{2}k_y\right). \tag{22}$$

s is the fixed length of the spin vectors ($\hbar = 1$).

A topological phase boundary is obtained by requiring two eigenvalues to be equal. At the K point of the Brillouin zone, e.g., at $\boldsymbol{k}_K = (-4\pi/3, 0)$, $\mathfrak{H}$ has the form

$$\mathfrak{H}(\boldsymbol{k}_K) = \begin{pmatrix} 0 & x & x^* \\ x^* & 0 & x \\ x & x^* & 0 \end{pmatrix} \tag{23}$$

with

$$x \equiv -(J_N + iD)s(1 + e^{2\pi i/3}) - 2J_{NN}s e^{2\pi i/3}. \tag{24}$$

Its eigenvalues are

$$\lambda_1 = 2\mathrm{Re}(x), \tag{25}$$

$$\lambda_{2,3} = -\mathrm{Re}(x) \pm \sqrt{3}|\mathrm{Im}(x)|. \tag{26}$$

Thus, the topological phase boundary in terms of the exchange parameters is given by

$$\frac{D}{J_N} = \sqrt{3}\left|2\frac{J_{NN}}{J_N} - 1\right|. \tag{27}$$

Since the degeneracy occurs at each K and K' point of the Brillouin zone, the Chern number of the associated bands changes by $\Delta C = \pm 2$ when crossing this boundary.

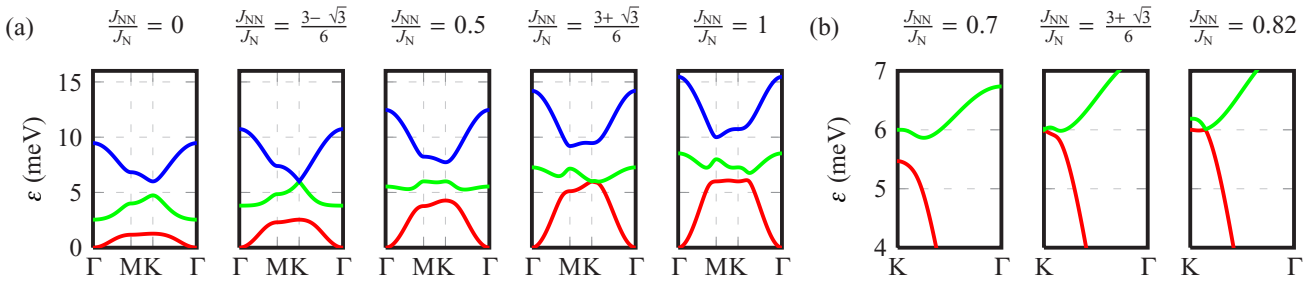

FIG. 5. (Color online) Magnon band structures of a kagome lattice for selected nearest- (N) and next-nearest- (NN) neighbor Heisenberg exchange parameters (as indicated). The Dzyaloshinskii-Moriya parameter D equals $J_N = 1$ meV. (a) Closing and reopening of a band gap at K, from left to right, according to the phase boundary given by Eq. (27). (b) Degeneracy along the Γ-K line. The bands are distinguished by colors.

A numerical analysis of the band structure (Fig. 5) yields two additional phase boundaries [Fig. 6(a)]: a linear and a nonlinear one. The latter approaches the boundary derived analytically as $J_{NN}/J_N \searrow 0.5$. All band degeneracies are located along the Γ-K and Γ-K' lines, respectively. These are parametrized by $\zeta \in [0,1]$ with $\zeta = 0$ and 1 for Γ and K, respectively [Fig. 6(b)]. The accumulation at the K point arises due to the analytically derived boundary, while the one at Γ is identified with the linear boundary in Fig. 6(a); the eigenvalue analysis of $\mathfrak{H}(0)$ results in

$$\frac{D}{J_N} = \sqrt{3}\left|\frac{J_{NN}}{J_N} + 1\right|. \tag{28}$$

The nonlinear boundary is associated with the descending curve in Fig. 6(b), indicating that this degeneracy moves along Γ-K and Γ-K' [cf. Fig. 5(b) for $D = J_N = 1$ meV and $J_{NN}/J_N = 0.82$]. Because this degeneracy appears six times within the first BZ the Chern numbers of the associated bands change by $\Delta C = \pm 6$. The additional phase boundary caused by a degeneracy at Γ is not of interest for the present study as it is located within the antiferromagnetic phase [Fig. 6(c); the antiferromagnetic phase is identified by negative magnon energies at nonzero $\boldsymbol{k}$]. The resulting topological phase diagram is given in Fig. 6(d).

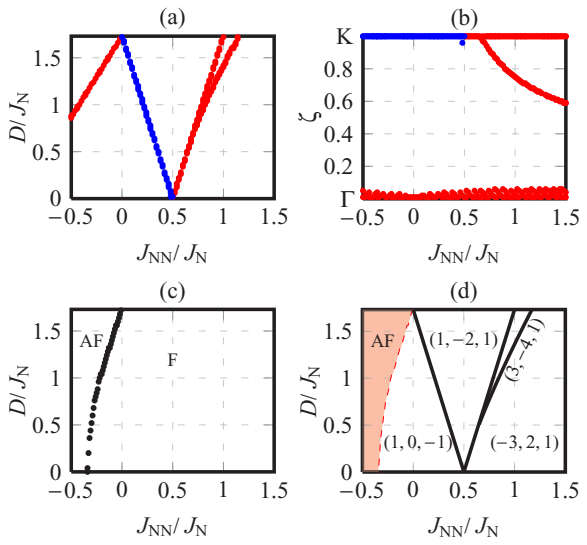

FIG. 6. (Color online) Analysis of band degeneracies. (a) Parameter combinations D/J_N and J_{NN}/J_N for which two neighboring bands are degenerate; red (blue) lines indicate degeneracy of the lower (upper) two bands 1 and 2 (2 and 3). (b) Point of degeneracy, ζ, along Γ-K line as a function of the parameter ratio J_{NN}/J_N. (c) Boundary between antiferromagnetic (AF) and ferromagnetic (F) phases. (d) Complete topological phase diagram with regions characterized by sets (C_1, C_2, C_3) of Chern numbers. The antiferromagnetic phase is colored red.

C. High-temperature limit of the transverse thermal conductivity

In this section we derive the high-temperature limit of the transverse thermal conductivity,

$$\kappa^{xy}_{\lim} \equiv \lim_{T\to\infty} \kappa^{xy}(T). \tag{29}$$

Although we disregard a ferromagnet-to-paramagnet transition and the influence of magnon-magnon interaction, it turns out that this quantity is helpful in describing MHE systems.

In the rewritten expression

$$\kappa^{xy}_{\lim} = \lim_{T\to\infty}\left(\frac{\kappa^{xy}(T)}{T}\Big/\frac{1}{T}\right), \tag{30}$$

both $\kappa^{xy}(T)/T$ and $1/T$ tend to zero because $c_2(\varrho(\varepsilon,T)) \to \pi^2/3$ for all ε and the sum of the Chern numbers of all bands vanishes, $\sum_i C_i = 0$. Thus,

$$\lim_{T\to\infty}\left(\frac{\kappa^{xy}(T)}{T}\right) = \frac{k_B^2}{2\pi\hbar}\frac{\pi^2}{3}\sum_i C_i = 0. \tag{31}$$

By means of l'Hôpital's rule it follows that

$$\kappa^{xy}_{\lim} = \lim_{T\to\infty}\left(-T^2\frac{\partial}{\partial T}\frac{\kappa^{xy}(T)}{T}\right) \tag{32}$$

$$= -\frac{k_B^2}{(2\pi)^2\hbar}\lim_{T\to\infty}\sum_i\int_{BZ} T^2\frac{\partial c_2(\varrho_i)}{\partial T}\Omega_i^z(\boldsymbol{k})\,dk^2, \tag{33}$$

with the final expression

$$\kappa^{xy}_{\lim} = -\frac{k_B}{(2\pi)^2\hbar}\sum_i\int_{BZ}\varepsilon_i(\boldsymbol{k})\Omega_i^z(\boldsymbol{k})\,dk^2. \tag{34}$$

Even though the high-temperature limit $T \to \infty$ will never be reached within the ferromagnetic phase, $\kappa^{xy}_{\lim}$ can be used

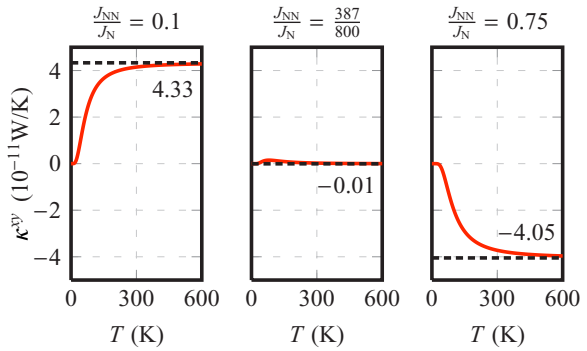

FIG. 7. (Color online) Transverse thermal conductivity κ^{xy} versus temperature T (solid lines) for $D/J_N = 1/4$ and selected ratios J_{NN}/J_N (as indicated), with $J_N = 4$ meV. The values of κ^{xy}_{lim} are given within each panel and represented by broken lines.

as a figure of merit to estimate the maximum magnitude of the thermal conductivity, because $\kappa^{xy}(T)$ rapidly approaches κ^{xy}_{lim} (Fig. 7). In the present cases, κ^{xy}_{lim} is reached at about $T = 300$ K. For the parameters $J_N = 4D = 4$ meV and $J_{NN}/J_N = 387/800$ the high-temperature conductivity is two orders of magnitude smaller than those for the other parameters shown in Fig. 7. The overall width of the conductivity as a function of temperature exceeds the limit insignificantly. A system's high-temperature-limit thermal conductivity is therefore a convenient approximation for the strength of its magnon Hall effect. Systems with high Curie temperature (i.e., of the order of room temperature for the presented results) allow for quantitative prediction as the limit is almost approached. It turns out, however, that for some regions in the phase space κ^{xy}_{lim} does not reproduce the correct sign of the thermal conductivity as a function of temperature, as will be discussed in the following paragraphs. Only the topological phases $(1,0,-1)$ and $(-3,2,1)$ show conductivities with the same sign as the associated high-temperature limit.

To motivate a relation of the high-temperature limit κ^{xy}_{lim} of the transverse thermal conductivity with the topological phase space, we assume a magnonic system with two flat bands; $\varepsilon_i(\boldsymbol{k}) = \bar{\varepsilon}_i$ $(i = 1,2)$. This approximation yields

$$\kappa^{xy}_{lim} \propto -\frac{1}{2\pi}\sum_{i=1}^{2}\bar{\varepsilon}_i \int_{BZ}\Omega^z_i(\boldsymbol{k})\,dk^2 = C_1\Delta\varepsilon, \qquad (35)$$

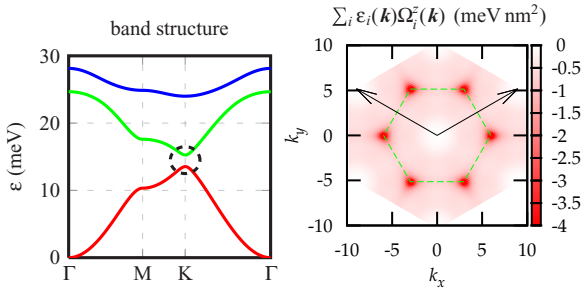

FIG. 8. (Color online) Band structure (left) and integrand of Eq. (34) (right). Arrows represent the reciprocal lattice vectors and the dashed green line indicates the Brillouin zone. $J_N = 10J_{NN} = 8D = 4$ meV.

where $\Delta\varepsilon = \bar{\varepsilon}_2 - \bar{\varepsilon}_1$ denotes the energy gap. This expression states that the sign of κ^{xy}_{lim} is given by the sign of the first band's Chern number C_1.

In the case of a kagome lattice the above constant-energy approximation is justified as follows. The integrand $\varepsilon_i(\boldsymbol{k})\Omega^z_i(\boldsymbol{k})$ contributes sizably to the entire integral mainly in regions of the BZ in which the Berry curvature is large (Sec. III A), that is, at avoided crossings as shown in Fig. 8. If there is a single avoided crossing in each irreducible part of the Brillouin zone (cf. the dashed circle in Fig. 8), the band structure can be approximated as constant at the avoided crossings (in contrast to two or more avoided crossings that are different in energy). By this approximation, κ^{xy}_{lim} reads

$$\kappa^{xy}_{lim} \propto \begin{cases} -(\bar{\varepsilon}_1 - \bar{\varepsilon}_3) > 0 & (1,0,-1), \\ -(\bar{\varepsilon}_1 - 2\bar{\varepsilon}_2 + \bar{\varepsilon}_3) & (1,-2,1), \\ -(3\bar{\varepsilon}_1 - 4\bar{\varepsilon}_2 + \bar{\varepsilon}_3) & (3,-4,1), \\ -(-3\bar{\varepsilon}_1 + 2\bar{\varepsilon}_2 + \bar{\varepsilon}_3) < 0 & (-3,2,1). \end{cases}$$

The sign is unique only within the phases $(1,0,-1)$ and $(-3,2,1)$ since $\bar{\varepsilon}_3 > \bar{\varepsilon}_2 > \bar{\varepsilon}_1$. In the other phases, the sign of the conductivity depends on the ratios of the energies $\bar{\varepsilon}_i$ and is not fixed. This, admittedly, crude approximation is corroborated by the numerical results shown in Fig. 9, where the line of vanishing high-temperature-limit conductivity is found within the phase $(1,-2,1)$.

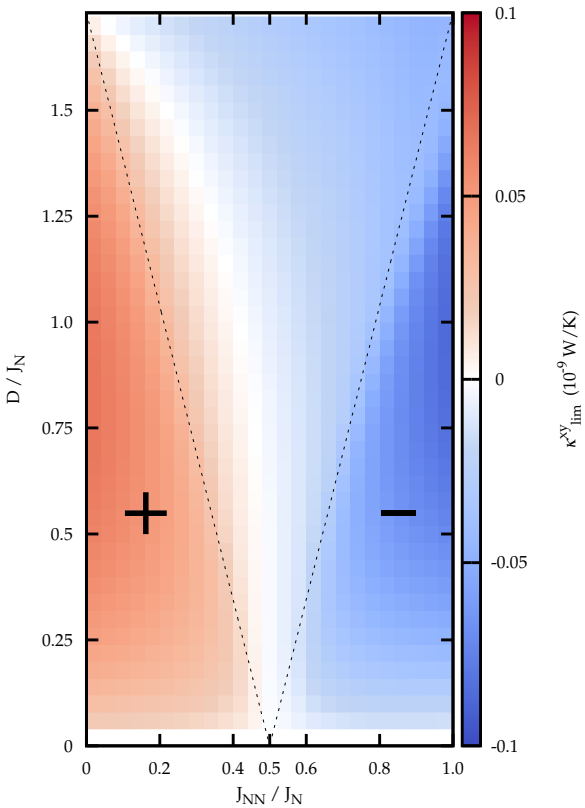

FIG. 9. (Color online) Topological phase diagram of the high-temperature transverse thermal conductivity κ^{xy}_{lim}, shown as color scale (right). Regions with positive (negative) values are marked + (−). The broken lines represent the analytically derived phase boundaries given by Eq. (27).

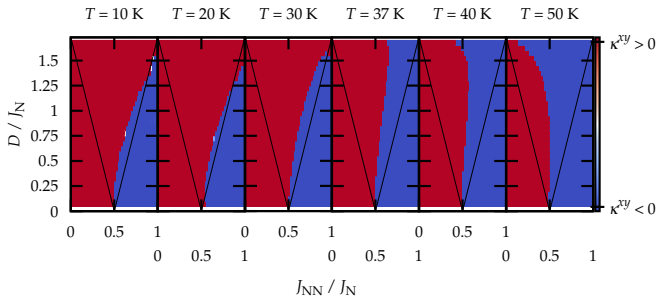

FIG. 10. (Color online) Sign of the transverse thermal conductivity κ^{xy} within the topological phase space for selected temperatures T (as indicated). $J_N = 4$ meV.

The above findings open up possibilities of changing a system's transverse thermal conductivity and heat current direction. Traversing through the phase diagram will lead to a change of the magnitude or even the sign of the thermal conductivity. Only systems with specific combinations of exchange parameters show a change of sign of the thermal conductivity with temperature. These combinations are located within the region that is covered by the line of zero κ^{xy} versus temperature (Fig. 10). In this phase-space region the conductivity shows a positive local maximum at low temperatures, although it converges to a negative limit (Fig. 11).

D. Application to $Lu_2V_2O_7$

Having studied the fundamental properties of the MHE in two-dimensional kagome lattices in the preceding sections, we proceed with an application to the three-dimensional pyrochlore $Lu_2V_2O_7$. Instead of considering a "true" three-dimensional lattice, we treat the system as a stack of non-interacting kagome layers. This allows the application of the methods derived so far, in particular the classification by Chern numbers [cf. the topological phase diagram in Fig. 6(d)].

To come closer to the experiment, the temperature dependence of the magnetization has to be considered. This could be done within a microscopic picture, that is, by considering the thermal fluctuations of the local spins which could enter the exchange parameters [25,26]. For the time being, we restrict ourselves to a macroscopic picture. To be more specific, we assume that the spins s scale with temperature in the same way as the magnetization,

$$s \to s\left(1 - \frac{T}{T_C}\right)^{\beta}, \tag{36}$$

with the critical temperature $T_C = 70$ K (Ref. [5]) and the critical exponent $\beta = 0.362$ (Ref. [27]).

From the Curie temperature T_C, the spin-wave stiffness $D_S = 21$ meV Å^2, and the lattice constant $a = 7.024$ Å, we determine the Heisenberg exchange parameter to $J_N = 3.405$ meV. J_{NN} is set to zero, so that there is no interaction between adjacent kagome planes.

To compare the thermal conductivity κ^{xy}_{2D} of a two-dimensional system with that of the associated three-dimensional one, κ^{xy}_{3D}, we introduce a characteristic length l which equals the spacing of (111) lattice planes. The red triangles in Fig. 1(a) suggest that l is twice as large as the height of a tetrahedron with an edge length of $a/2$; hence, $\kappa^{xy}_{3D} = \kappa^{xy}_{2D}/l$ with $l = \sqrt{6}a/3$.

Now we compare the theoretical transverse thermal conductivity with its experimental counterpart [5], with the strength D of the DM interaction as the only parameter. For realistic values of D, $Lu_2V_2O_7$ is within the $(1,0,-1)$ topological phase and exhibits a MHE with positive transverse thermal conductivity, in agreement with experiment.

The comparison is shown in Fig. 12, for two selected values of $D = \sqrt{6}/2\widetilde{D}$ [cf. Eq. (6)]. The magnetic field was chosen slightly larger than the saturation field determined by Onose *et al.* (Ref. [5]). Reasonable agreement is found for $\widetilde{D}/J_N = 0.39\%$–$0.56\%$, that is, for parameters two orders of magnitude smaller than those deduced by Onose *et al.*, who derived $\widetilde{D}/J_N = 32\%$. A density functional calculation for

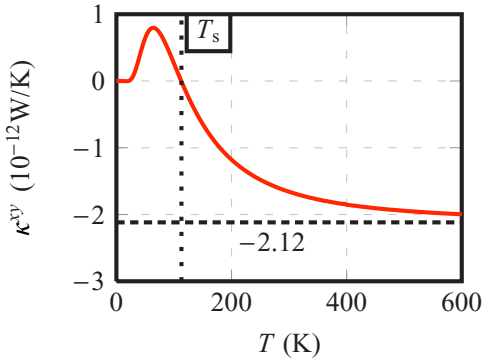

FIG. 11. (Color online) Transverse thermal conductivity κ^{xy} versus temperature T for $J_{NN}/J_N = 1/2$, $D/J_N = 1/4$, and $J_N = 4$ meV (solid line). The dashed line represents the limit $\kappa^{xy}_{lim} = -2.12 \times 10^{-12}$ W/K; the dotted line marks the temperature $T_s = 113$ K of vanishing conductivity.

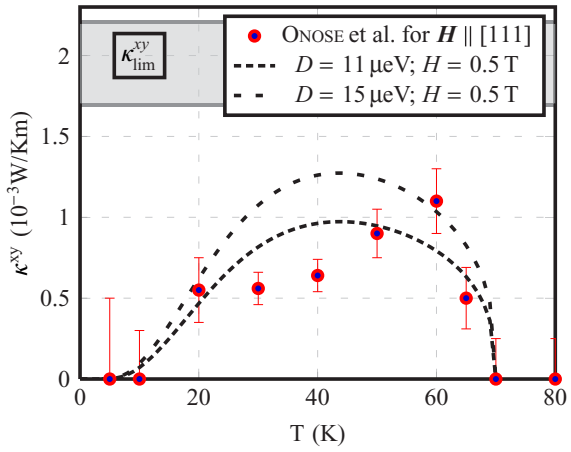

FIG. 12. (Color online) Transverse thermal conductivity κ^{xy} of $Lu_2V_2O_7$ versus temperature T. Theoretical data for Dzyaloshinskii-Moriya interactions $D = 11$ μeV (dashed line) and 15 μeV (wide-dashed line) are compared with experimental data from Ref. [5] (dots). The external magnetic field of 0.5 T is chosen slightly larger than the saturation field in the experiment. The range of the high-temperature limits of κ^{xy} is indicated by the gray area.

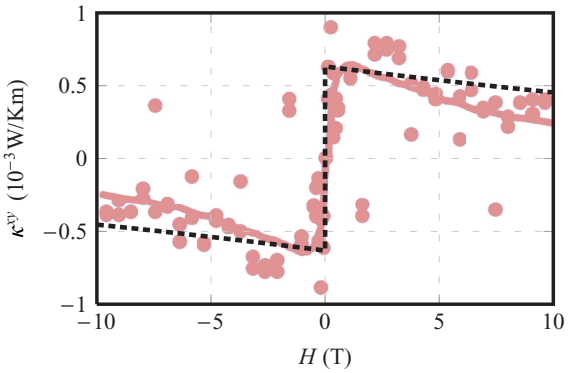

FIG. 13. (Color online) Transverse thermal conductivity κ^{xy} of $Lu_2V_2O_7$ versus applied magnetic field H along [111] at $T = 20$ K. The theoretical result has been obtained for Dzyaloshinskii-Moriya interaction $D = 15$ μeV (broken line). Experimental data (red dots) for the magnetic field direction along [100] are reproduced from Ref. [5].

$Y_2V_2O_7$, which possesses magnetic properties similar to those of $Lu_2V_2O_7$, by Xiang *et al*. (Ref. [28]), yields $\widetilde{D}/J_N = 5\%$.

We attribute the mismatch between our $\widetilde{D}/J_N$ ratio and the one obtained in Ref. [5] to the approximation of the three-dimensional systems by a stacking of noninteracting kagome planes. For example, disregarding the fourth basis atom of the pyrochlore basis reduces the bandwidths of the magnons; as a consequence, avoided crossings which give the major contributions to the conductivity are too low in energy. Thus, the c_2 function is too large, which has to be compensated by a reduced DM interaction.

In contrast, the approximation in Ref. [5] causes an overestimation of the DM interaction: in a model for a pyrochlore lattice, only contributions of the lowest-energy band at the Γ point (Goldstone mode) have been considered. Thus, the sizable contributions of the avoided crossings at higher energies are omitted (cf. Fig. 3). This approximation is valid for very small temperatures, as is evident from the rapid decrease of c_2; it is questionable for elevated temperature because c_2 is sizable at higher energies (compare $T = 1$ K with $T = 23$ K in Fig. 2). We recall that the experimental data used for estimating D/J in Ref. [5] were taken at $T = 20$ K, for which c_2 cannot be safely neglected at the avoided crossings. To compensate for the missing contributions, the value of the Berry curvature around the Γ point is estimated too large and so the DM constant $\tilde{D}$ is overestimated.

Neither the approximation in Ref. [5] nor ours takes into account magnon-magnon or magnon-phonon interactions which may influence the transverse thermal conductivity of $Lu_2V_2O_7$ at temperatures close to its Curie temperature. The mismatches of the $\widetilde{D}/J_N$ ratio can be explained by the approximations discussed in the preceding paragraphs.

Finally, we address the dependence of the transverse thermal conductivity on the strength of the applied magnetic field (Fig. 13). The experimental data were obtained for a magnetic field applied in the [100] direction, in contrast to theory ([111] direction), thus complicating a quantitative analysis. Nevertheless, the overall trend—namely, the gradual decrease of the conductivity (in absolute value) for increasing magnetic field—is reproduced. It is explained by the Zeeman term in the Hamiltonian [Eq. (10)] which shifts the entire magnonic band structure towards larger energies and, therefore, to regions with smaller c_2 (Fig. 2).

IV. OUTLOOK

Having analyzed kagome lattices in this paper, an evident extension of our study is to pyrochlore crystals in which all exchange interactions are considered. An important issue is the negative transverse thermal conductivity of $In_2Mn_2O_7$ (Ref. [29]), in contrast to the positive ones of $Lu_2V_2O_7$ and $Ho_2V_2O_7$; this needs to be explained by a topological phase diagram. With a phase diagram at hand, one should be able to predict systems with a strong magnon Hall effect.

It appears of great interest to find a kagome system with exchange parameters that are located in a region in which the conductivity changes sign. In this paper we have given a recipe for such a material. Its overall transverse thermal conductivity is, however, one order of magnitude smaller than that of $Lu_2V_2O_7$, which calls for advanced measurement techniques.

[1] C. L. Chien and C. R. Westgate, *The Hall Effect and Its Applications* (Plenum, New York, 1980).
[2] *CRC Handbook of Thermoelectrics*, edited by D. M. Rowe (CRC Press, Boca Raton, FL, 1995).
[3] R. S. Popovic, *Hall Effect Devices* (IOP Publishing, London, 2004).
[4] C. Strohm, G. L. J. A. Rikken, and P. Wyder, Phys. Rev. Lett. **95**, 155901 (2005).
[5] Y. Onose, T. Ideue, H. Katsura, Y. Shiomi, N. Nagaosa, and Y. Tokura, Science **329**, 297 (2010).
[6] R. Matsumoto and S. Murakami, Phys. Rev. Lett. **106**, 197202 (2011).
[7] R. Matsumoto and S. Murakami, Phys. Rev. B **84**, 184406 (2011).
[8] L. Zhang, J. Ren, J.-S. Wang, and B. Li, Phys. Rev. B **87**, 144101 (2013).
[9] H. Hasan and C. Kane, Rev. Mod. Phys. **82**, 3045 (2010).
[10] X.-L. Qi and S.-C. Zhang, Rev. Mod. Phys. **83**, 1057 (2011).
[11] M. Z. Hasan and J. E. Moore, Annu. Rev. Condens. Matter Phys. **2**, 55 (2011).
[12] D. Xiao, M.-C. Chang, and Q. Niu, Rev. Mod. Phys. **82**, 1959 (2010).
[13] R. Resta, Rev. Mod. Phys. **66**, 899 (1994).
[14] W. Heisenberg, Z. Phys. **49**, 619 (1928).
[15] I. Dzyaloshinsky, J. Phys. Chem. Solids **4**, 241 (1958).
[16] T. Moriya, Phys. Rev. **120**, 1 (1960).
[17] F. J. Dyson, Phys. Rev. **102**, 1217 (1956).
[18] Y. Yoshida, S. Schröder, P. Ferriani, D. Serrate, A. Kubetzka, K. von Bergmann, S. Heinze, and R. Wiesendanger, Phys. Rev. Lett. **108**, 087205 (2012).
[19] M. Elhajal, B. Canals, R. Sunyer, and C. Lacroix, Phys. Rev. B **71**, 094420 (2005).

[20] V. N. Kotov, M. Elhajal, M. E. Zhitomirsky, and F. Mila, Phys. Rev. B **72**, 014421 (2005).
[21] H. Katsura, N. Nagaosa, and P. A. Lee, Phys. Rev. Lett. **104**, 066403 (2010).
[22] F. D. M. Haldane, Phys. Rev. Lett. **61**, 2015 (1988).
[23] M. V. Berry, Proc. R. Soc. London, Ser. A **392**, 45 (1984).
[24] P. Barone, T. Rauch, D. Di Sante, J. Henk, I. Mertig, and S. Picozzi, Phys. Rev. B **88**, 045207 (2013).
[25] D. Böttcher, A. Ernst, and J. Henk, J. Magn. Magn. Mater. **324**, 610 (2012).
[26] A. Szilva, M. Costa, A. Bergman, L. Szunyogh, L. Nordström, and O. Eriksson, Phys. Rev. Lett. **111**, 127204 (2013).
[27] C. Holm and W. Janke, Phys. Rev. B **48**, 936 (1993).
[28] H. J. Xiang, E. J. Kan, M. H. Whangbo, C. Lee, S.-H. Wei, and X. G. Gong, Phys. Rev. B **83**, 174402 (2011).
[29] T. Ideue, Y. Onose, H. Katsura, Y. Shiomi, S. Ishiwata, N. Nagaosa, and Y. Tokura, Phys. Rev. B **85**, 134411 (2012).